JOURNAL OF MATERIALS SCIENCE **35** (2000) 5681 – 5690

A technique for the determination of interfacial properties from debond length measurement

YONGJIAN SUN, R. N. SINGH
Department of Materials Science and Engineering, University of Cincinnati, P.O. Box 210012, Cincinnati, OH 45221-0012, USA
E-mail: rsingh@uceng.uc.edu

Fiber-matrix interfacial debonding is observed and the debond length is directly measured during flexure tests performed on transparent SiC fiber-reinforced borosilicate glass composites. The relationship among the debond length, applied stress, and interfacial properties is investigated both experimentally and theoretically. A new technique based on debond length measurement is introduced for measuring fiber-matrix interfacial properties such as interfacial shear strength, frictional shear stress, and interfacial debond energy. Analytical models are employed for the new technique to interpret the experimental data. Fiber pushout technique is also employed to measure the interfacial properties independently. It is shown that these two different techniques of debond length measurement and fiber pushout test for measuring the interfacial properties can provide comparable results.

1. Introduction

The mechanical properties of fiber-reinforced ceramic composites such as first matrix cracking stress and toughness are strongly dependent on the properties of fibers, matrix materials, and fiber/matrix interface. Generally, a weakly bonded interface is desirable for a tough ceramic matrix composite because of the toughening mechanism associated with the processes of fiber bridging, fiber/matrix interface debonding, and fiber pullout. Therefore, the methods for characterizing interfacial properties are important for the evaluation of composite performance. A number of different techniques including microindentation [1, 2], fiber pushout [3, 4], single fiber pullout [5, 6], matrix crack spacing measurement [7], and Raman or fluorescence spectroscopy [8, 9] techniques have been developed for measuring the fiber/matrix interfacial properties such as interfacial shear strength, frictional shear stress, and interfacial debond energy. The other interfacial properties such as interfacial roughness, residual stress at the interface because of the thermal expansion mismatch, and coefficient of friction have also been investigated [10–12]. Using these techniques, the influences of fiber coating and coating thickness on the interfacial properties have been studied as well [1, 10]. In comparison to these techniques, fiber pushout and microindentation are most easily performed and give the most direct measurements. But, the complexity arises because the fiber is loaded under compression which differs from the real case. Single fiber pullout, however, is limited by the difficulties in preparing samples. Microindentation method sometimes is limited by the difficulty in determining the machine compliance, which can be of the order of magnitude of the indenter displacement.

Along with these techniques, several analytical models have been developed. Marshall and Oliver [1] proposed a load-displacement relationship for microindentation technique. Singh and Sutcu [3] and Shetty [4] provided models for fiber pushout. Kerans and Parthasarathy [6] derived expressions to relate the characteristic load (peak load and load drop) with the displacement and interfacial properties. In some of the models, the roughness of the interface and misfit anisotropy [6, 12] are also taken into consideration. In all of these approaches, the load-displacement data are generated and used to calculate the interfacial properties from models based on the considerations of the interfacial debonding and frictional sliding. Therefore, such factors as machine compliance, sample alignment, and loading rate strongly affect the load-displacement relationship. It is also not difficult to find that in all of these techniques the debond length is a term frequently used to describe the load-displacement relationship. However, it is difficult to directly measure the debond length because of the visual inaccessibility of the debond length measurement in most ceramic composites.

One of the objectives of this study is to characterize the process of interfacial debonding in a transparent glass composite, record and measure the debond length, and correlate this measurement of the debond length to the interfacial properties. Analytical models which describe the relationship between the interfacial properties and debond length are employed to calculate the interfacial properties. Finally, fiber pushout tests are performed on the same composites to determine the interfacial properties which are then compared with similar values measured from the debond length measurements to validate this debond length approach for determining interfacial properties.

2. Experimental procedure

2.1. Sample preparation

Borosilicate F glass (Corning Glass Work Inc., NY) was used as a matrix material, and SiC SCS-6 fibers (Textron Specialty Materials, MA) were used as a reinforcement material to fabricate a transparent glass composite. These monofilaments were fabricated by CVD technique in which SiC was deposited on a carbon core of 37 μm diameter, followed by depositions of two layers of carbon-rich coatings of 3 μm thickness. The overall fiber diameter is about 142 μm. The material properties are listed in Table I. These materials were selected to have similar expansion characteristics in order to minimize the residual stresses upon composite fabrication.

Transparent composites with close-to-full density were fabricated by Tape Casting/Binary Sintering (TCBS) method [13]. The unidirectional composites made for this study had 12% fibers by volume. After grinding, cutting, and polishing, two groups of samples were prepared. The samples used in debond length measurement tests were flexure bars with the dimension of $3.3 \times 1.4 \times 50$ mm^3, and those used in fiber pushout tests were thin slices from 0.2 to 0.5 mm in thickness. The mechanical properties of these composites are listed in Table II.

2.2. Debond length measurement technique

Flexure tests were performed using an Instron mechanical testing system to induce interfacial debonding. A schematic of the test setup is illustrated in Fig. 1. The outer span was 40 mm and the inner span was 20 mm. The crosshead speed was about 0.2 mm/min. Matrix cracking occurred on the tensile surface of a flexure bar when the applied load increased beyond the matrix cracking stress. Accompanying matrix cracking, interfacial debonding was also created if the interface was weakly-bonded [2]. This debond phenomenon can be observed in a transparent glass matrix composite [14, 15]. In order to measure the dependency of the debond length on the applied load/stress, a typical flexure test was stopped at different levels of stress, as

TABLE I Mechanical properties of SiC fiber and F glass

Materials	Elastic Modulus (GPa)	Strength (GPa)	Failure Strain (%)	$\alpha^\dagger$ ($\times 10^{-6}/°C$)
SCS-6	400	3.4	0.8 - 1.0	4.23 [13]
F glass*	56	0.056	0.1	4.25

*The composition for F glass is 76% $SiO_2 \cdot 16\% B_2O_3 \cdot 8\% K_2O$, obtained from Corning Glass Works, Corning, NY.

$^\dagger\alpha$ is the coefficient of thermal expansion (25 °C to 500 °C).

TABLE II Parameters and properties for SCS-6 fiber reinforced borosilicate glass composite

Fiber volume fraction, V_f	0.12
Elastic modulus of composite, E_c (GPa)	97.3[a]
Matrix porosity (%)	1 - 2 [13]
K_{Ic} of glass matrix (MPa $\sqrt{m}$)	0.77 [15]
FMC stress, σ_{FMC} (MPa)	90 [13]
Ultimate strength, σ_{cu} (MPa)	440 [13]

[a] Calculated by rule of mixture.

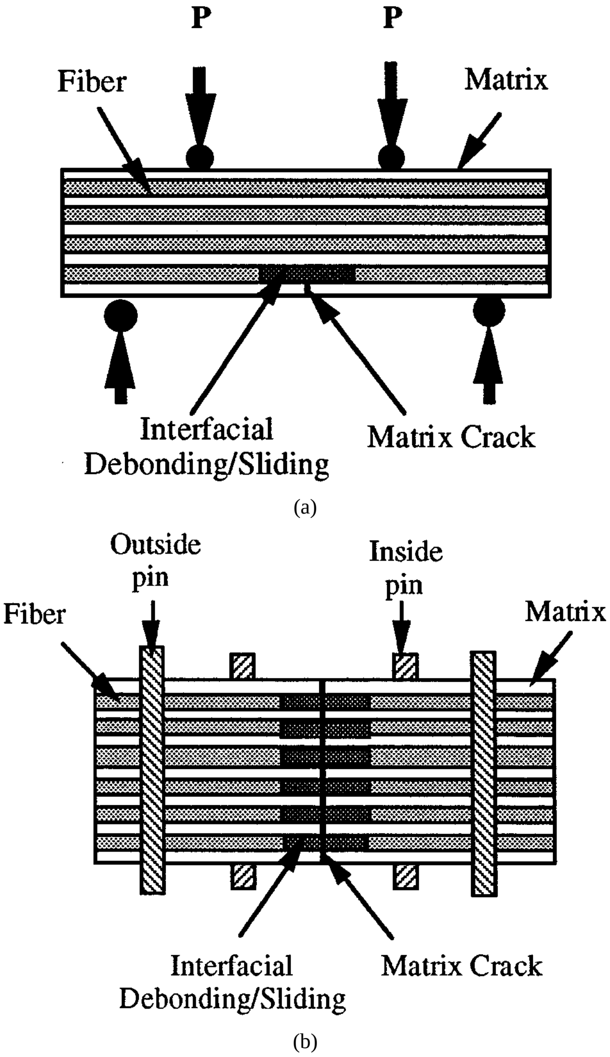

Figure 1 Schematic diagram for debond length measurement technique. (a) A side view of experimental setup; (b) A view at the bottom tensile surface.

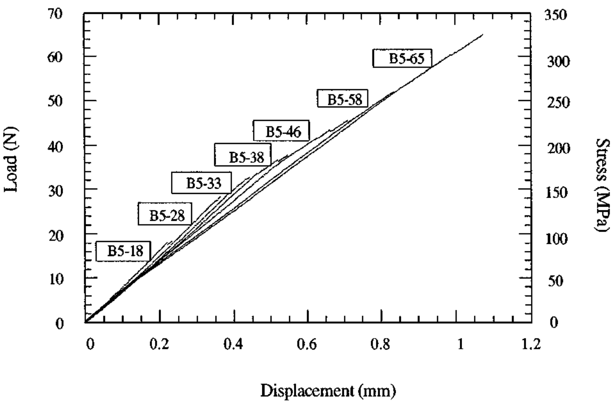

Figure 2 The load-displacement curves for a composite loaded to different stress levels (For example, B5-18 denotes the sample B5 loaded at 18 N).

shown in Fig. 2, and the debond length was directly measured at each level of stress using a video imaging system. The stress was calculated based on the beam theory. The relationship between the debond length and applied stress was then used to determine interfacial properties. The analytical models used for this study are also described later in this paper. The advantages of debond length measurement technique to determine interfacial properties include: a) the machine compliance does not influence the results, b) the tensile load produced on the outer surface of a bend bar in this technique is more prototypic of the real composite when stressed, and c) this approach is more realistic because the experiments are conducted on the whole composite instead on a single fiber, as is customary in fiber pullout or pushout tests to determine interfacial properties.

2.3. Fiber pushout technique

As an alternative technique, fiber pushout was also used to determine and compare the interfacial properties. Fig. 3 shows a schematic diagram of the fiber pushout test. These experiments were conducted using a Micro Measure Machine (Process Equipment Company, OH) at a loading rate of 10 N/min. The pushout probe, made of Tungsten Carbide, was about 100 μm in diameter. The machine compliance was measured by pushing a fully dense bulk alumina plate of 5 mm in thickness. The real fiber displacement during a pushout test was obtained after subtracting the machine compliance. A typical load-displacement curve for a fiber pushout test is shown in Fig. 4. From the load-displacement curve, the initiation point (point A in Fig. 4) of interfacial debonding, the peak load (point B) at which the interfacial debonding has propagated through the sample thickness, and the load drop (point C) corresponding to the beginning of a steady-state interfacial sliding can be measured. Therefore, the interfacial properties such as interfacial shear strength, debond energy, and frictional shear stress can be obtained from such a load-displacement data. In some cases after fiber pushout, fiber pushback tests were also performed on the already pushed fibers. The load required for fiber pushback can also be used to determine the frictional sliding stress and this then can be compared to the values obtained from the load-displacement curves.

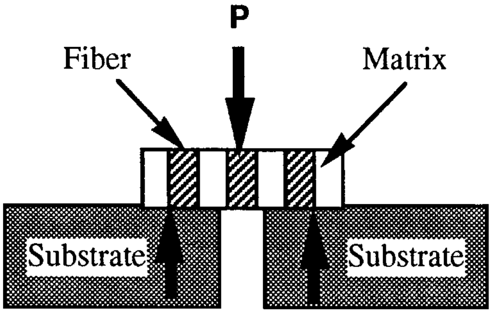

Figure 3 Schematic diagram of fiber pushout test.

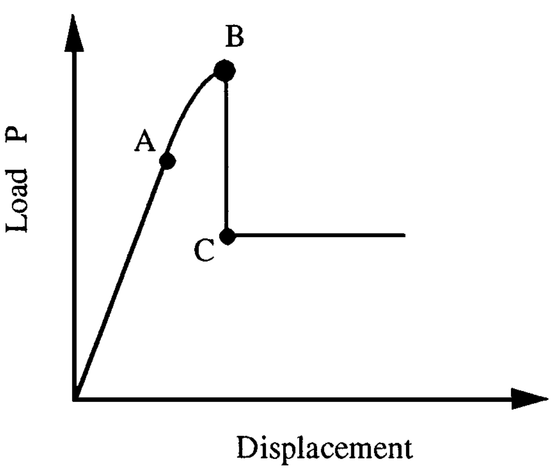

Figure 4 A representative load-displacement curve for a fiber pushout test.

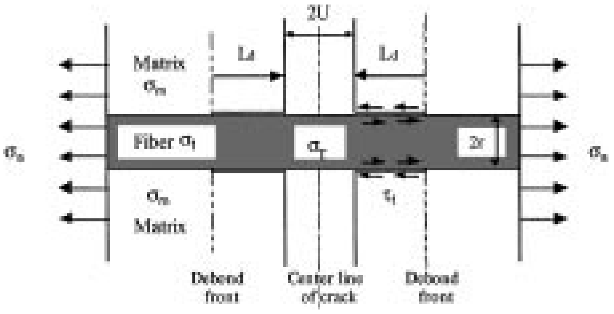

Figure 5 Schematic of interfacial debonding and fiber pullout.

2.4. Analytical models for debond length measurement technique

The micromechanism of interfacial debonding has been studied by several researchers [16–22]. A composite subjected to external stress will experience shear stress at the interface which can lead to interfacial debonding if the applied stress is sufficiently high (after matrix cracking). For a cracked composite with a debonded interface of length L_d, as shown in Fig. 5, the dependence of the debond length on the interfacial properties and applied stress can be expressed by two different models: a force balance approach and the energy balance approach. The force balance approach is well described by Hutchinson and Jensen (HJ) [16], Marshall [17], and Budiansky, Evans and Hutchinson (BEH) [18]. The initiation and propagation of the interfacial debonding requires that the interfacial shear stress is larger than the interfacial shear strength. Thus, the stress-debond length dependence can be obtained as [16, 18]

$$\frac{L_\mathrm{d}}{r} = \left(\frac{V_\mathrm{m}E_\mathrm{m}}{V_\mathrm{f}E_\mathrm{c}}\right)\frac{\sigma_\mathrm{a} - \sigma_\mathrm{i}}{2\tau_\mathrm{f}} \tag{1}$$

where V, E denote the volume fraction and elastic modulus, respectively, subscripts m, f, c denote the matrix, fiber, and composite, respectively, r is the fiber radius, and τ_f is the interfacial frictional shear stress, σ_a is the applied stress on composite, and σ_i is a characteristic applied stress named the initiation stress for interfacial debonding or sliding. σ_i is strongly dependent on the fiber/matrix interfacial properties. For a frictionally coupled interface, σ_i can be simplified as sliding initiation stress σ_slide [18], which depends on the coefficient of friction and normal clamping stress at the fiber/matrix interface. However, for a strongly bonded interface, this initiation stress is referred to as a debond initiation stress σ_d. σ_d is related to the cohesive shear strength of the interface, τ_d, by the following relationship [18]:

$$\sigma_d = \left(\frac{2V_f E_c}{\rho V_m E_m} \right) \tau_d \tag{2}$$

where ρ is the shear-lag parameter determined by the following formula $\rho^2 = \frac{4E_c G_m}{V_m E_m E_f \varphi}$, where G_m is the shear modulus of the matrix and $\varphi = \frac{2 \ln V_f + V_m(3-V_f)}{2V_m^2}$. The cohesive shear strength of the interface, τ_d, is then related to the interfacial debond energy Γ_d by the following expression [18]:

$$\tau_d = \sqrt{\frac{4G_m \Gamma_d}{r\varphi}} \tag{3}$$

It is worth noting that for a frictionally-coupled interface, Γ_d is equal to zero, thus τ_d is equal to zero. The fiber/matrix interface is then controlled by the frictional shear stress, τ_f.

In comparison to the force balance approach, the debond length dependency on the interfacial properties and applied stress from the energy balance approach is not extensively analyzed. The basic criterion for debond initiation and growth is that the energy release rate during interfacial debonding is sufficiently large to balance the energy required for the generation of new debonded surfaces and dissipation of frictional energy along the interface. This criterion was employed by Li, Shah, and Mura [19], Sutcu and Hillig [20], and Hsueh [21] to correlate the load-displacement and first-matrix-cracking behavior to the interfacial debonding. Hsueh [21] found that the dependency of the debond length on the applied stress derived from energy balance approach was identical to the results derived from the strain mismatch and strength based criterion (force balance approach in this paper). Li, Shah and Mura [19], however, obtained a different expression between the debond length and applied stress by assuming that strain energy in bonded portion is not changed during the process of interfacial debonding (which may be incorrect):

$$\frac{L_d}{r} = \frac{\sigma_a}{2\tau_f V_f} \left\{ 1 - \left[\frac{V_f E_f}{E_c} + \frac{V_m E_m}{E_c} \left(\frac{\sigma_d}{\sigma_a} \right)^2 \right]^{1/2} \right\} \tag{4}$$

where σ_d is dependent on the interfacial debond energy Γ_d by the following relationship:

$$\sigma_d = V_f \left(\frac{4\Gamma_d E_f}{r} \right)^{1/2} \tag{5}$$

It is not difficult to see the differences between the results obtained by Li *et al.* [19] and BEH [18] or HJ [16] or Hsueh [21]. These differences are discussed later.

From Equations 1 and 4 above, the interfacial debond initiation stress σ_d can be obtained by curve fitting the debond length-stress data because this stress value corresponds to the threshold stress with zero debond length. Once σ_d is obtained, functions $F(\sigma_a)$ and $G(\sigma_a)$ can be redefined to simplify Equations 1 and 4. For the force balance approach Equation 1 is redefined as,

$$F(\sigma_a) = \frac{V_m E_m r}{2V_f E_c}(\sigma_a - \sigma_d) \tag{6}$$

and

$$L_d = \frac{F(\sigma_a)}{\tau_f} \tag{7}$$

For the energy balance approach Equation 4 can be redefined as,

$$G(\sigma_a) = \frac{\sigma_a r}{2V_f} \left\{ 1 - \left[\frac{V_f E_f}{E_c} + \frac{V_m E_m}{E_c} \left(\frac{\sigma_d}{\sigma_a} \right)^2 \right]^{1/2} \right\} \tag{8}$$

and

$$L_d = \frac{G(\sigma_a)}{\tau_f} \tag{9}$$

Hence, the frictional shear stress τ_f can be obtained from the slope of the linear curves associated with the dependence of the debond length on the functional parameters $F(\sigma_a)$ and $G(\sigma_a)$. It is worth noting that the values of $2\pi r F(\sigma_a)$ and $2\pi r G(\sigma_a)$ can be physically termed as the effective driving forces for the interfacial frictional sliding. Comparing the functional parameters $F(\sigma_a)$ with $G(\sigma_a)$, it is found that $F(\sigma_a)$ is larger than $G(\sigma_a)$ by $\frac{V_m E_m r}{4V_f E_c}\sigma_a(1 - \frac{\sigma_d}{\sigma_a})^2$. When the applied stress σ_a is equal to σ_d, the debond crack may initiate and the difference between $F(\sigma_a)$ and $G(\sigma_a)$ becomes zero. However, with the increase of applied stress σ_a, both the debond length L_d and the difference between $F(\sigma_a)$ and $G(\sigma_a)$ will increase. Therefore, the effective driving force for interfacial sliding based on the energy balance criterion (Li's Model) is smaller than the force balance criterion (BEH and HJ).

The debond energy Γ_d is also computable from Equations 2, 3, and 5 as long as σ_d is available. This is the approach that has been taken in this study to determine interfacial properties from debond length measurements.

3. Results and discussion

3.1. Debond length measurement

Experiments to measure interfacial debond length were conducted on five specimens. The typical load-displacement curves for specimens loaded to various load levels is shown in Fig. 2. The first matrix crack was detected at 18 N (85 MPa, corresponding to the first matrix crack stress). Debonding phenomenon was observed by white band when the first matrix crack occurred. With the increase of the applied stress, multiple matrix cracks were created. The sequence of creation and distribution of these matrix cracks is shown in Fig. 6. The numbers on the dashed lines from 1 to 16 in Fig. 6 indicate the sequence of matrix crack generation. The magnitude of the load/stress, written horizontally along the various crack numbers, indicates the load/stress at which these cracks were created. For example, the first three cracks 1, 2, 3 were detected at a load of 18 N (85 MPa, corresponding to the first matrix cracking), and cracks 15, 16 were generated at a load of 46 N (217 MPa, corresponding to the saturation of matrix cracking). No additional matrix cracks were observed beyond a load of 46 N (217 MPa). The debond length increased with the applied load as shown in Fig. 7a–d. These results are plotted in Fig. 8 which shows the dependencies of the debond length on the applied stress for six different matrix cracks. The dependence of the average debond length on the applied stress is also displayed in Fig. 8.

A close to linear debond length-stress relationship was displayed for these matrix cracks before the saturation stress of 217 MPa was reached at which the debonded zones from either sides of the uncracked matrix block reached each other. The difference in debond length values between crack # 9 and crack # 12 resulted from the non-uniformity of the matrix crack distribution and mutual debond interactions. The intercept of the linear curves with the applied stress axis upon extrapolation was used to obtain the interfacial debond initiation stress σ_d. This threshold stress is determined as about 50 MPa. Based on the experimental data and analytical models, the values of functional parameters $F(\sigma_a)$ (force balance approach) and $G(\sigma_a)$ (energy balance approach) at different levels of applied stress were calculated. These results were then used to determine the new relationships between the average debond length and functional parameters $F(\sigma_a)$ and $G(\sigma_a)$, as shown in Fig. 9. The slopes of these two curves provide values of the τ_f for the force balance and energy balance approaches, respectively. The interfacial debond shear strength τ_d and debond energy Γ_d calculated from Equations 2, 3, and 5 using the debond length measurements are listed in Table III. The differences in values

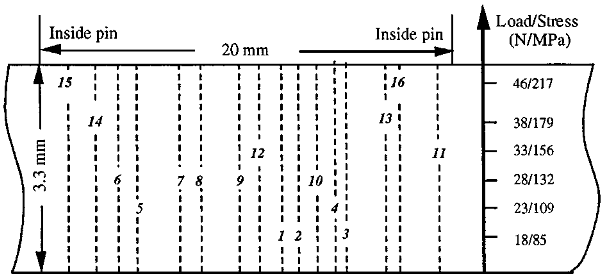

Figure 6 Evolution and distribution of matrix cracks on the tensile face of the specimen.

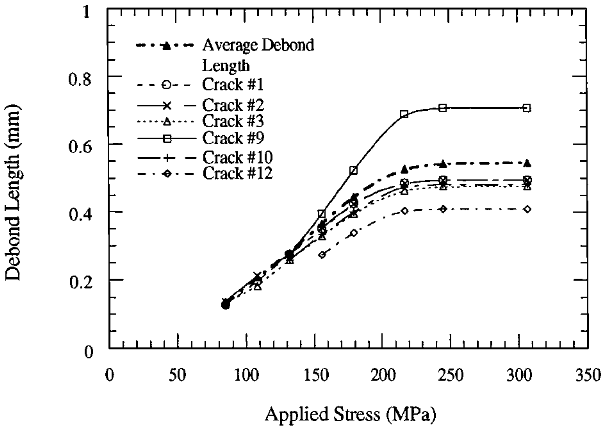

Figure 8 The dependence of debond length on the applied stress for six different matrix cracks.

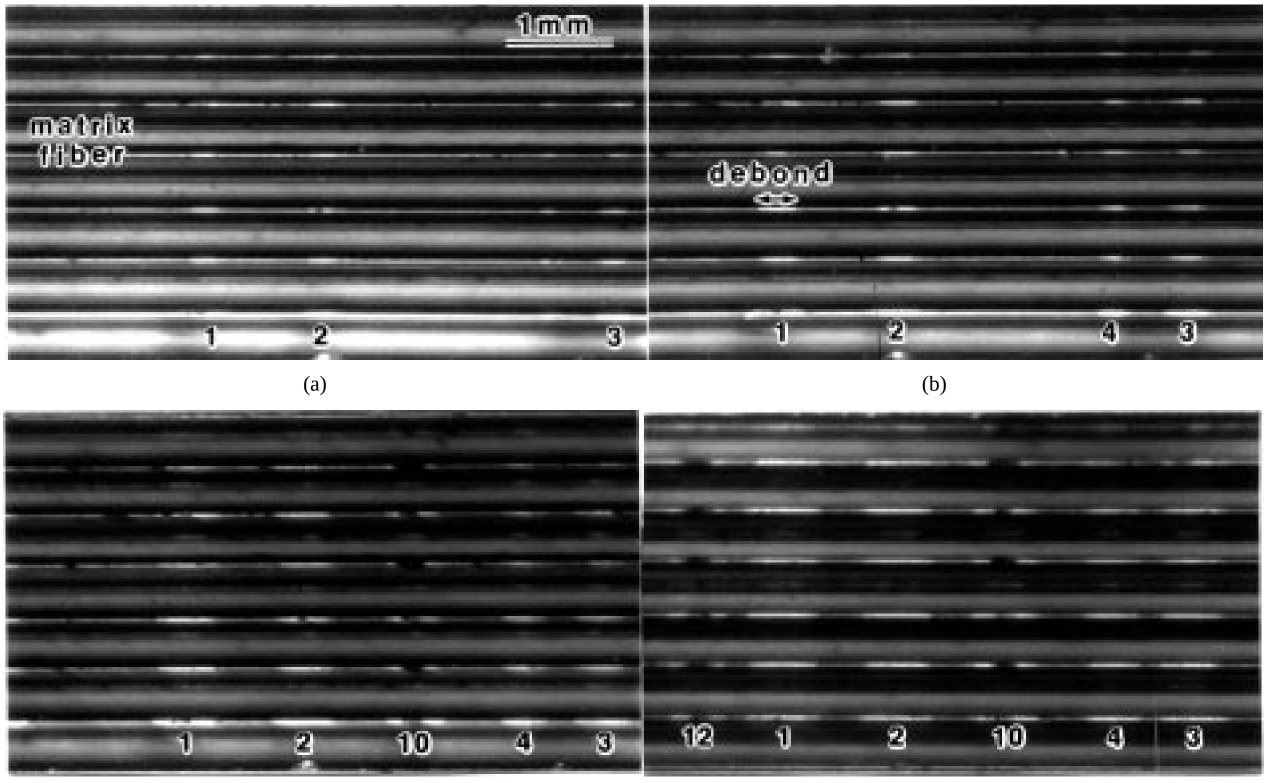

(a)

(b)

(c)

(d)

Figure 7 Optical micrographs showing the progression of debonding (patterns) with increasing applied load. (a) Cracks# 1, 2, 3 at 18 N; (b) Cracks# 1, 2, 3, 4 at 23 N; (c) Cracks# 1, 2, 3, 4, 10 at 28 N; (d) Cracks# 1, 2, 3, 4, 10, 12 at 33 N.

TABLE III Interfacial properties determined by the debond length measurement technique

	Debond Length Measurement	
Interfacial Properties	BEH/HJ (Force Balance)	Li, etc. (Energy Balance)
Interfacial frictional stress, τ_f (MPa)	48 ± 3 (Equation 7)	30 ± 2 (Equation 9)
Debond initiation stress, σ_d (MPa)	50 ± 3	50 ± 3
Interfacial shear strength, τ_d (MPa)	70 ± 6[b]	70 ± 6[b]
Debond energy, Γ_d (J/m^2)	2.9 ± 0.3[c]	3.85 ± 0.4 (Equation 5)

[b] Calculated from Equation 2.
[c] Calculated from Equation 3.

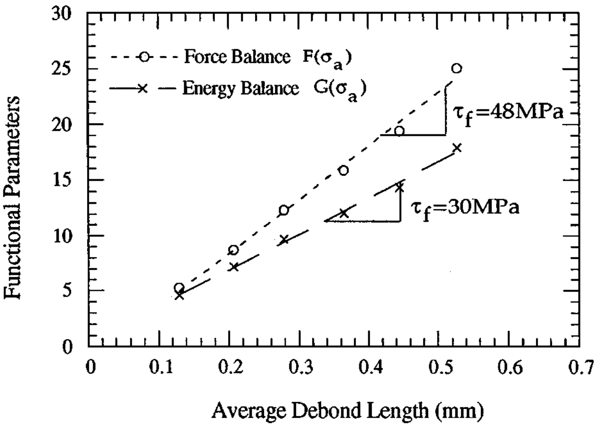

Figure 9 The linear dependency of debond length on the functions $F(\sigma_a)$ and $G(\sigma_a)$.

of interfacial properties measured this way result from the discrepancy in models derived based on different approaches and assumptions. For instance, the interfacial frictional sliding stress obtained from the HJ, BEH and Hsueh's models (Equations 6 and 7) is about 1.6 times the stress value obtained from Li's model (Equations 8 and 9).

According to the fundamental fracture mechanics, a mode-II debond crack will generate and propagate not only when the interfacial shear stress is larger than the interfacial shear strength, but also when the energy release rate in the elastic body is sufficient for creating new debonded surfaces and for dissipating frictional energy. The frictional sliding stress, frictional energy dissipation, and frictionally-induced shear strain energy (not included in all mentioned models) all contribute to the process of debonding. They contribute to the effective driving force for interfacial frictional sliding. For example, when the debond length is very short, the frictional dissipation energy plays little role compared with the interfacial debond energy. The effective driving force for interfacial frictional sliding is mainly determined by the interfacial debond energy. Therefore, the effective driving forces for interfacial frictional sliding calculated from the energy balance and force balance approaches are very close (the initial points at a debond length less than 0.13 mm, as shown in Fig. 9). But, with the increase of debond length, the frictional dissipating energy increases while the debond energy term still remains the same. The frictional dissipation energy can not be ignored after a certain extension of the debond length which then contributes largely to the suppression of the effective driving force for interfacial frictional sliding (a lower value of $G(\sigma_a)$ compared to $F(\sigma_a)$, as shown in Fig. 9), thus making it possible for a lower frictional sliding stress (obtained from Equations 8 and 9) to stop the debond propagation. Therefore, the energy balance criterion for debonding process seems stricter in this irreversible debonding process than the force balance criterion. Consequently, the interfacial property values obtained from energy balance approach may be more reasonable.

In addition, the discrepancies among interfacial properties listed in Table III can also result from different assumptions in these models. For instance, both Hsueh [21] and Li [19] used the same energy balance criterion. However, their expressions of debond length-applied stress relation were different. This implies that further investigation and analysis using the energy balance criterion may be needed.

3.2. Fiber pushout

Single fiber pushout tests were performed on composites to determine interfacial properties. A typical load-displacement curve, after subtracting the machine compliance of this study, is shown in Fig. 10. There are three characteristic points in Fig. 10: A, B, and C. The load-displacement curve shows a linear dependence up to point A, the debond initiation point. After point A, the data started to deviate from a linear behavior. This deviation from linear behavior is clearly shown in Fig. 11 which is still the same data as in Fig. 10 but on an expanded scale. The debond initiation stress σ_d (to be consistent with the debond initiation stress measured by the debond length measurement technique) at point A was about 57 MPa if calculated using the following expression:

$$\sigma_d = V_f \frac{P_A}{\pi r^2} \tag{10}$$

where P_A is the load value at point A.

With the increase of pushin stress, the interfacial debonding propagated. This was verified by the continuous decrease of the slope in the load-displacement

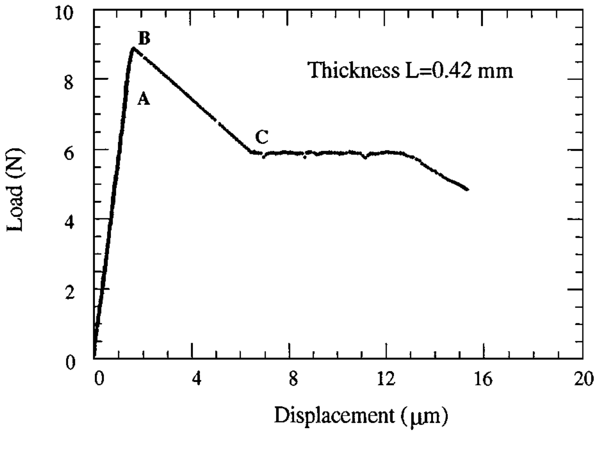

Figure 10 A representative load-displacement curve in fiber pushout.

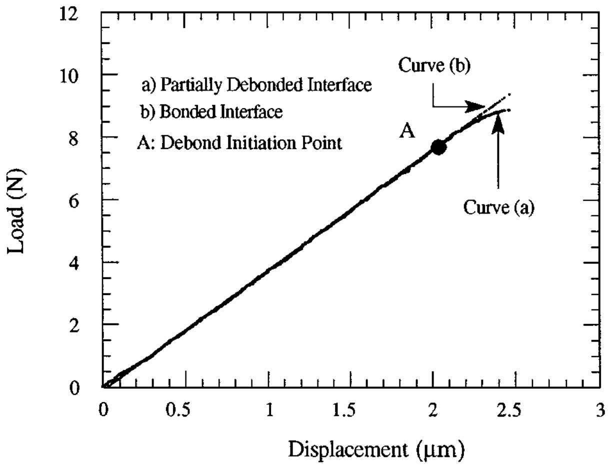

Figure 11 The deviation from linearity of the load-displacement curve because of the interfacial debonding.

curve after point A, as shown in Fig. 11. The peak load at point B is a complicated load value which corresponds to the complete debonding of the fiber/matrix interface, and is associated with the debond energy, sample thickness, and end effect of the thin sample. Therefore, it may be inappropriate to relate this value to the interfacial properties. However, a shear-lag analysis of a pushout test is still available to determine the interfacial shear strength, τ_d, by the following expressions [4, 23]:

$$P_B = \frac{2\pi r}{\rho}\tau_d \tanh(\rho L) \approx 2\pi r L \tau_d \qquad (11)$$

where P_B is the peak load value at point B, ρ is the shear-lag parameter, and L is the length of the embedded fiber. The interfacial shear strength τ_d can be calculated from Equation 11 as 50 MPa. Because of the total failure of the interface bond, the force balance is destroyed because of missing σ_d in Equation 1 and can not be restored by friction right away. The energy which was associated with the bond and stored in the elastic body was suddenly released which led to a large increase in displacement and a sudden drop in load.

This unstable state was finally stabilized by the interfacial frictional force and dissipation of frictional energy which created a steady state shown by point C. This steady state was established basically by a balance between the push-in force and frictional shear force, which can be expressed as [4, 23]

$$P_c = \frac{\pi r^2 \sigma_0}{k}\left[1 - \exp\left(-\frac{2\mu k L}{r}\right)\right] \approx 2\pi r L \tau_f \quad (12)$$

where P_c is the load value at point C, σ_0 is the compressive (clamping) stress on the fiber, μ is the coefficient of friction characterizing the sliding friction at the interface, and k is a nondimensional parameter determined by $k = \frac{E_m \nu_f}{E_f(1+\nu_m)}$. The approximation given by Equation 12 is valid because the high exponential terms of a series expansion are negligible because L is relatively small in this study. Therefore, the interfacial frictional stress calculated from Equation 12 is about 33 MPa.

Fig. 12 shows scanning electron micrographs of fiber pushout samples. Fig. 12a shows the top surface of a pushout sample from which fiber was pushed into the matrix, and Fig. 12b shows the bottom surface of a sample after fiber pushout. There was no matrix crack on the top surface of the sample but a few radial matrix cracks were observed on the bottom surface. This was produced because of the weak glass matrix and some type of bonding between the fiber and matrix. A close look at the pushout sample revealed that the interfacial debonding occurred between the outermost fiber coating (carbon) and glass matrix, as shown in Fig. 13. It was also found in Fig. 14 that some fiber coating debris remained on the glass matrix wall after the fiber pushout because of the interfacial bonding between the fiber coating and matrix.

In order to verify that the measured interfacial frictional shear stress was because of the frictional sliding at the interface, the pushed-out fibers were pushed back. A typical load-displacement curve for the fiber pushback is shown in Fig. 15. The values obtained from fiber pushback was about 17 MPa, which was smaller than the value calculated from point C in Fig. 10. This lower value of the interfacial frictional shear stress might be explained by Fig. 16 which displays a damaged sample surface after fiber pushback. Some other reasons for a lower value can be that during the first push the mechanically interlocked fiber/matrix interface was damaged which led to a lower roughness/coefficient of friction at the interface, and the normal matrix clamping stress on the fiber was partially relaxed due to the process of matrix cracking after the first push. Therefore, the frictional sliding stress obtained from fiber pushback tests is expected to be lower for these composites.

3.3. Comparison of the interfacial properties measured by debond length measurement and fiber pushout

The interfacial properties independently measured by the debond length measurement and fiber pushout are listed in Tables III and IV, respectively. These results show that the SCS-6 SiC fiber reinforced glass matrix composites possess a slightly stronger fiber/matrix interface with a higher frictional sliding stress as compared to the values measured by other researchers [4, 23, 24]. Mostly reported interfacial shear strength, τ_d, for SCS-6 fiber reinforced borosilicate glass matrix composites ranged from 4–30 MPa [5, 24], and the frictional sliding stress, τ_f, for this group of composites ranged from 3–10 MPa [2, 4]. The higher values of the interfacial shear strength and frictional sliding stress could be attributed to two aspects of the TCBS

TABLE IV Interfacial properties determined by the fiber pushout technique

Interfacial Properties	Fiber Pushout	
Interfacial frictional stress, τ_f (MPa)	33 ± 4 (Equation 12)	
Debond initiation stress, σ_d (MPa)	57 ± 5 (Equation 10)	
Interfacial shear strength, τ_d (MPa)	78 ± 7[b]	50 ± 4 (Equation 11)
Debond energy, Γ_d (J/m^2)	3.6 ± 0.5[c]	1.5 ± 0.2[c]

[b] Calculated from Equation 2.
[c] Calculated from Equation 3.

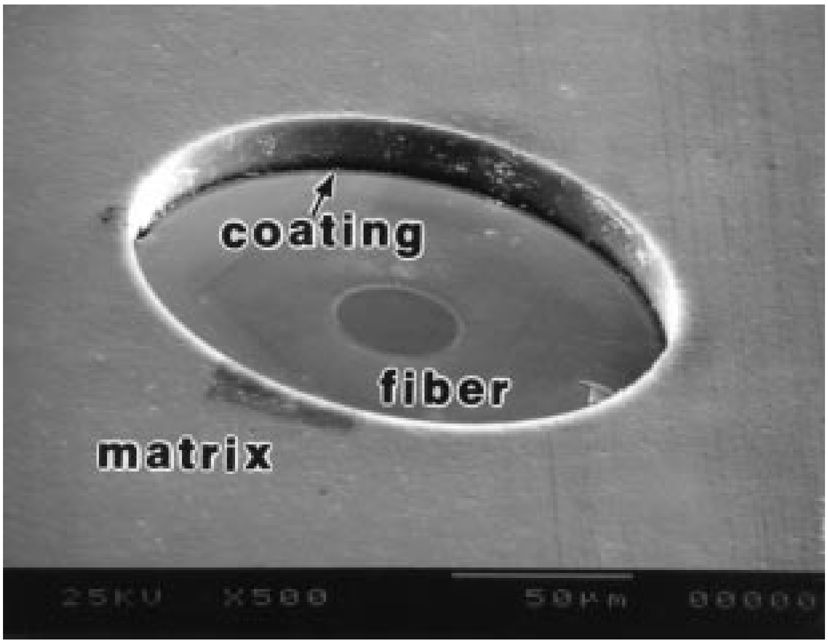

(a)

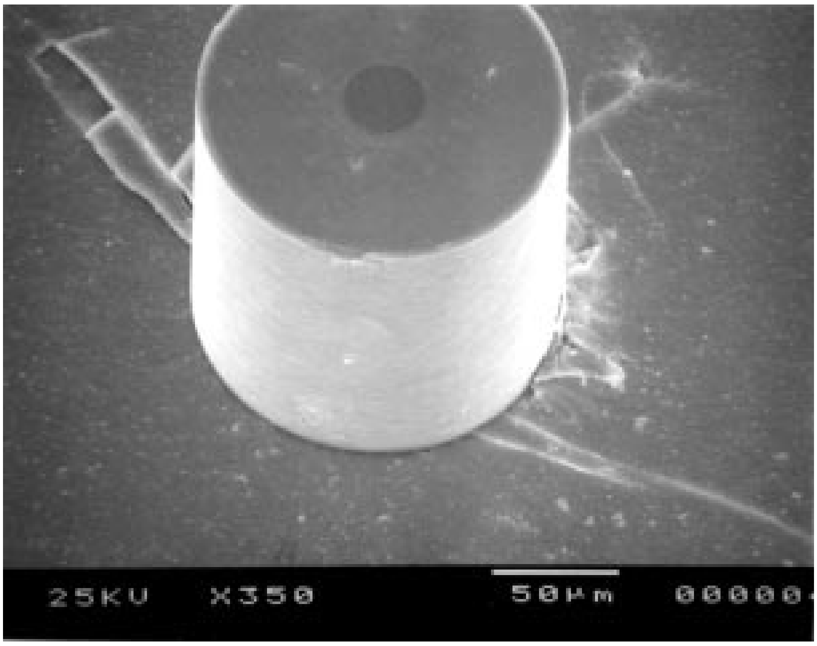

(b)

Figure 12 (a) The top surface of a sample with a fiber being pushed in; (b) The bottom surface of a sample with a fiber being pushed out.

[13] processing method in this study. Firstly, TCBS is different from other methods such as hot pressing [4, 5, 23] and melt forming [4]. Particularly, to produce a transparent glass composite of this study, an oxidizing treatment in air for binder burnout was given. Secondly, argon gas of a low purity was introduced at above 920°C to achieve a full density during sintering. Both procedures were expected to oxidize the SCS-6 fiber resulting in a slightly stronger fiber-matrix interface, as observed in this study.

The interfacial properties obtained from debond length measurement and fiber pushout tests are in a reasonable agreement. The validity of fiber pushout technique as a predominant method for interfacial characterization was verified by this independent debond length measurement method. This new debond length measurement technique differs itself from other techniques such as fiber pullout and microindentation in its special approach. However, it is very interesting to find that the interfacial properties measured by these two techniques are also slightly different, which may provide additional information about the techniques. The debond initiation stress σ_d, and frictional shear stress τ_f measured from fiber pushout tests were higher than those measured by the debond length measurement technique (especially the energy balance approach). This difference can be partially explained by analyzing the contribution of the Poisson's ratio effect on the interfacial properties. In debond length measurement, a fiber is under tension (axial pulling) along the fiber axis, and the poison ratio effect of a axially-pulled fiber on the interface is to offset the residual radial compressive (clamping) stress.

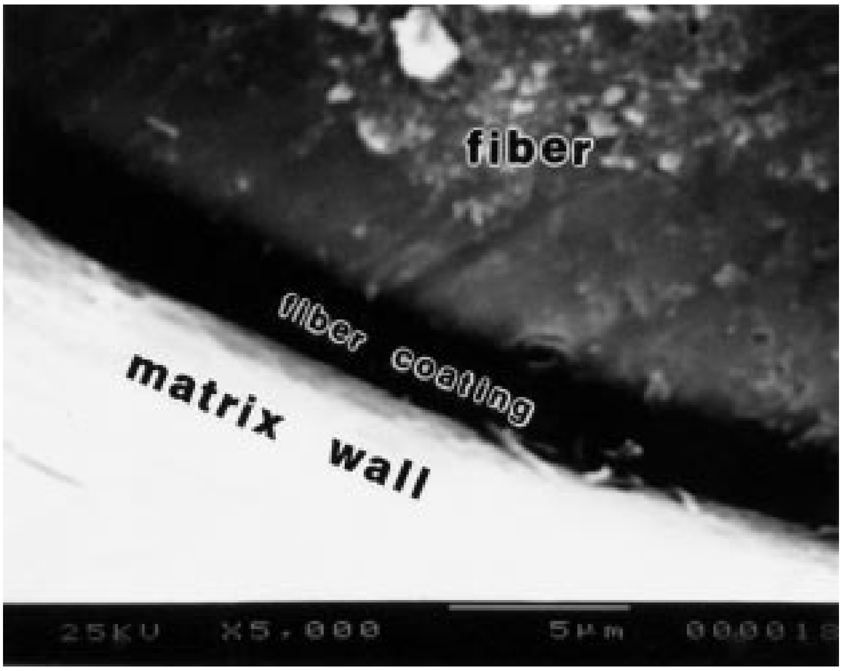

Figure 13 SEM observation of the remaining fiber coating of about 2.5 μm thickness after fiber pushout test.

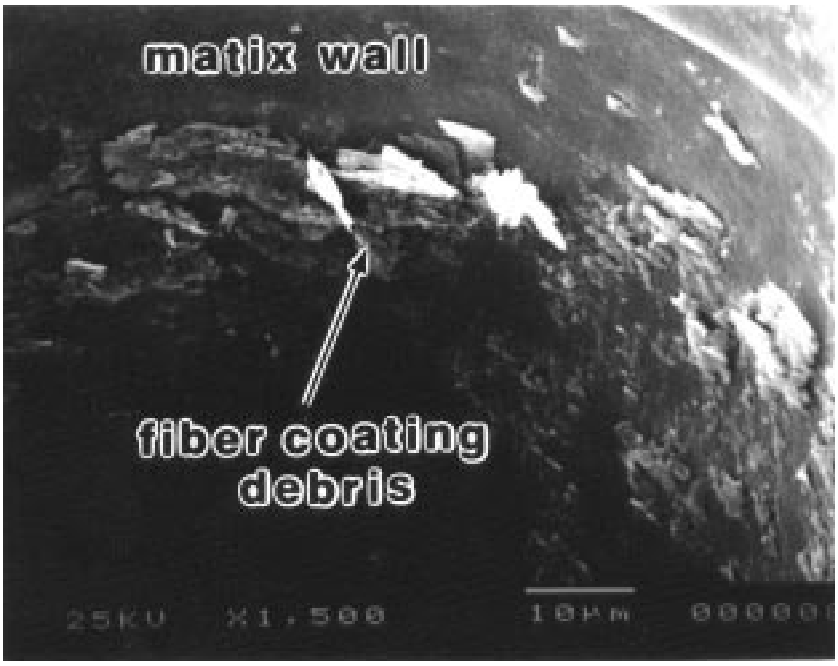

Figure 14 The residual debris of fiber coating on a matrix wall after fiber pushout test showing some type of interfacial bond.

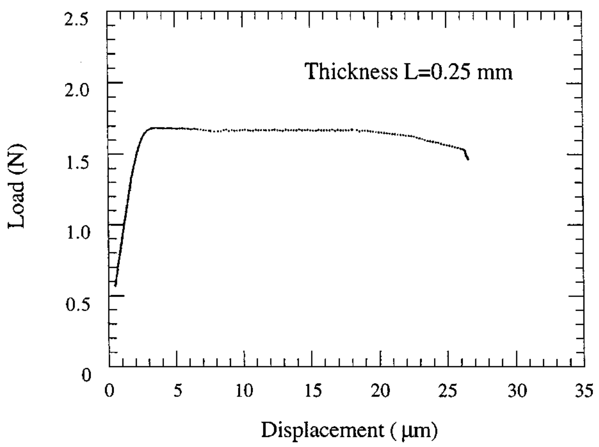

Figure 15 A load-displacement curve during fiber pushback showing a steady-state frictional sliding.

However, in a fiber pushout test, a fiber is under compression (pushing) along the fiber axis, and the Poisson's ratio effect of an axially-pushed fiber on the interface results in a radial compression at the interface. The frictional sliding stress, τ_f, is determined by the normal compressive stress σ_0 and coefficient of friction μ at the interface. Therefore, a higher value of τ_f from fiber pushout test is reasonable.

4. Summary

The micromechanism of interfacial debonding was investigated in a fiber-reinforced glass matrix composite. A close-to-linear relationship between the debond length and applied stress was found before saturation of the multiple matrix cracking. This debond length-applied stress relationship was used as a new approach

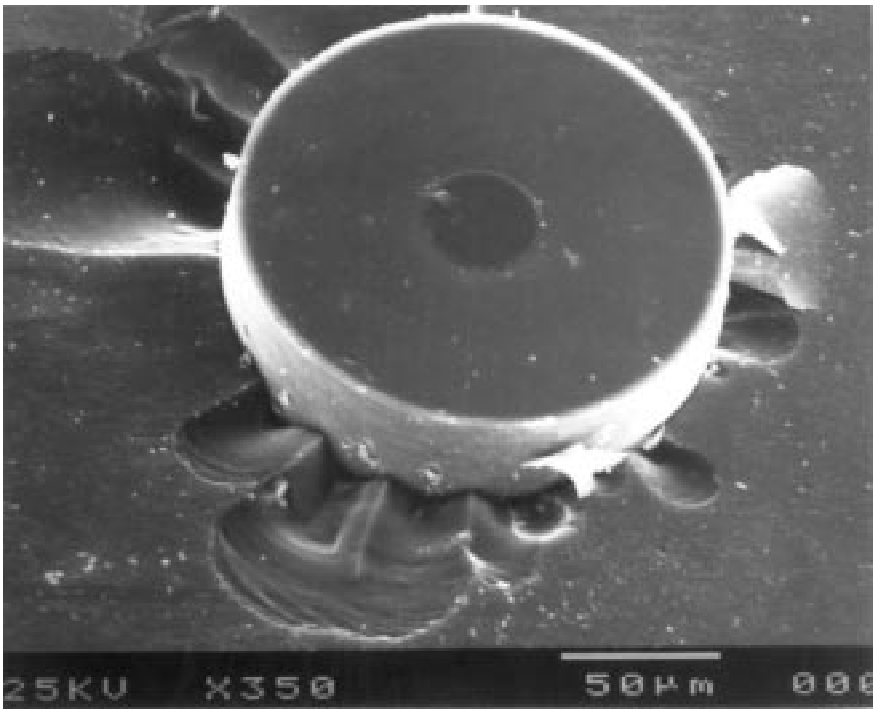

Figure 16 A damaged top surface after conducting a fiber pushback test.

to determine the fiber/matrix interfacial properties. Two analytical models, based on either the force balance or the newly-derived energy balance approaches, were used to analyze the experimental data. The influences of the models on the final results were also briefly discussed.

Interfacial properties were also measured independently by the fiber pushout technique, and the results were found to be comparable to the results obtained from the debond length measurement. This similarity verified the effectiveness and validity of the debond length measurement.

Acknowledgment

Authors are grateful to Dr. James Webb's design of polishing fixture for preparing fiber pushout sample, and to Dr. Susmit Kumar for discussions of the theoretical models. This research was supported by National Science Foundation through Grant #CMS-9625750.

References

1. D. B. MARSHALL and W. C. OLIVER, *J. Am. Ceram. Soc.* **70** (1987) 542.
2. D. H. GRANDE, J. F. MANDELL and K. C. C. HONG, *J. Mater. Sci.* **23** (1988) 311.
3. R. N. SINGH and M. SUTCU, *ibid.* **26** (1991) 2547.
4. J. D. BRIGHT and D. K. SHETTY, *J. Am. Ceram. Soc.* **72** (1989) 1891.
5. R. W. GOETTLER and K. T. FABER, *Composites Science and Technology* **37** (1989) 120.
6. R. J. KERANS and T. A. PARTHASARATHY, *J. Am. Ceram. Soc.* **74** (1991) 1585.
7. J. AVESTON, G. A. COOPER and A. KELLY, in National Physical Laboratory Conference, Nov. 4th UK, 1971.
8. X. YANG, D. J. BANNISTER and R. J. YOUNG, *J. Am. Ceram. Soc.* **79** (1996) 1868.
9. Q. MA and D. R. CLARKE, *Acta Metall. Mater.* **41** (1993) 1817.
10. R. N. SINGH and S. K. REDDY, *J. Am. Ceram. Soc.* **79** (1996) 137.
11. P. D. JERO, R. J. KERANS and T. A. PARTHASARATHY, *ibid.* **74** (1991) 2793.
12. D. B. MARSHALL, M. C. SHAW and W. L. MORRIS, *Acta Metall. Mater.* **43** (1995) 2041.
13. Y. J. SUN and R. N. SINGH, *Advances in Ceramic-Matrix Composites III, Ceramic Transactions* **74** (1996) 141.
14. D. R. MUMM and K. T. FABER, *Acta Metall. Mater.* **43** (1995) 1259.
15. Y. J. SUN and R. N. SINGH, *ibid.* **46** (1998) 1657.
16. J. W. HUTCHINSON and H. M. JENSEN, *Mechanics of Materials* **9** (1990) 139.
17. D. B. MARSHALL, *Acta Metall. Mater.* **40** (1992) 427.
18. B. BUDIANSKY, A. G. EVANS and J. W. HUTCHINSON, *Int. J. Solids Structures* **32** (1995) 315.
19. S. LI, S. P. SHAH, Z. LI and T. MURA, *ibid.* **30** (1993) 1429.
20. M. SUTCU and W. B. HILLIG, *Acta Metall. Mater.* **38** (1990) 2653.
21. C. HSUEH, *Acta Mater.* **44** (1996) 2211.
22. L. ZHOU, J. KIM and Y. MAI, *J. Mater. Sci.* **27** (1992) 3155.
23. R. KERANS, R. HAY, N. PAGANO and T. PARTHASARATHY, *Ceramic Bulletin* **68** (1989) 429.
24. A. JUREWICZ, R. KERANS and J. WRIGHT, *Ceram. Eng. Sci. Proc.* **10** (1989) 925.

Received 20 May 1999
and accepted 7 April 2000